

Hydrogen Effects on an Amorphous Fe-Si-B Alloy

N. ELIAZ and D. ELIEZER

Hydrogen absorption in and desorption from an amorphous $\text{Fe}_{80}\text{B}_{11}\text{Si}_9$ alloy, hydrogen effects on the microstructure of this alloy, and the possible mechanism of hydrogen embrittlement (HE) in this alloy have been studied. Ribbons were electrochemically charged with hydrogen at room temperature. The interaction of hydrogen with structural defects and the characteristics of hydrogen desorption were studied by means of thermal desorption spectroscopy (TDS). The effects of hydrogen on the microstructure and thermal stability were studied using X-ray diffraction (XRD), transmission electron microscopy (TEM), electrical resistivity measurements, and differential scanning calorimetry (DSC). The phenomenon of HE was investigated using scanning electron microscopy (SEM) and various mechanical testing techniques. The absence of hydride-forming elements resulted in low hydrogen solubility and low desorption temperatures. Hydrogenation at room temperature is reported for the first time to lead to either local nanocrystallization of the amorphous phase or transformation of nanocrystalline phases such as $\text{Fe}_{\sim 3.5}\text{B}$, originally present in the uncharged material, to a new nanocrystalline Fe_{23}B_6 phase. The susceptibility of this alloy to HE is explained in terms of high-pressure bubble formation.

I. INTRODUCTION

HYDROGEN interaction with amorphous alloys has been studied extensively due to both scientific and technological interest.^[1] In the framework of a more comprehensive investigation of hydrogen interaction with amorphous and quasicrystalline $\text{Zr}_{69.5}\text{Cu}_{12}\text{Ni}_{11}\text{Al}_{7.5}$ alloys, hydrogen effects on amorphous $\text{Fe}_{80}\text{B}_{11}\text{Si}_9$ were studied as well, for comparison.^[2] As $\text{Fe}_{80}\text{B}_{11}\text{Si}_9$ does not contain hydride-forming elements, the effect of chemical composition on hydrogen interaction with amorphous alloys may be estimated by comparing results for this alloy to results for an amorphous $\text{Zr}_{69.5}\text{Cu}_{12}\text{Ni}_{11}\text{Al}_{7.5}$ alloy. The $\text{Fe}_{80}\text{B}_{11}\text{Si}_9$ alloy belongs to the group of amorphous alloys composed of late transition metals (LTM) and metalloids (M). The ratio LTM:M (atomic concentrations) in this group is usually 80:20. Bennett *et al.*^[3] suggested that this ratio results from the filling of all large Bernal holes with the smaller and softer metalloid atoms to stabilize the random configuration.

The aim of this article is to present results on hydrogen absorption in and desorption from an amorphous $\text{Fe}_{80}\text{B}_{11}\text{Si}_9$ alloy. In addition, hydrogen effects on the microstructure, as well as the characteristics and mechanism of hydrogen embrittlement (HE) in this alloy, are discussed in detail. Finally, the effects of metalloids on hydrogen diffusion are briefly discussed, applying a new model to simulate the diffusion behavior of hydrogen in dilute amorphous Fe-H, Fe-Si-H, and Fe-B-H alloys, as described in detail elsewhere.^[4] In a recent complementary article,^[5] the authors applied laser-induced shock-wave measurements to determine the dominant mechanism of HE in an amorphous $\text{Fe}_{80}\text{B}_{11}\text{Si}_9$ alloy and to estimate the effects of the high pressures involved in cathodic charging. Therefore, these results are not presented within the present article.

II. EXPERIMENTAL DETAILS

Ribbons ($\sim 25\text{-}\mu\text{m}$ thick) of amorphous $\text{Fe}_{80}\text{B}_{11}\text{Si}_9$ were used for this research. The ribbons were produced by planar-flow casting and were kindly supplied by AlliedSignal Inc. (Parsippany, NJ). It is well known that various surface phenomena may affect the interaction of hydrogen with materials. For amorphous alloys, crystalline phases were detected near the surface of the ribbon that had not been in contact with the rotating wheel during melt spinning.^[6] Furthermore, surface-oxide layers were reported to hinder the desorption of hydrogen from an amorphous $\text{Zr}_{69.5}\text{Cu}_{12}\text{Ni}_{11}\text{Al}_{7.5}$ alloy.^[7] Hence, Auger electron spectroscopy/X-ray photoelectron spectroscopy (AES/XPS) experiments were carried out in this research before hydrogen charging, in order to compare the chemical composition of both sides of the ribbon. The results indicated that both were slightly oxidized.^[2] By means of optical microscopy, entrapped gas blisters were identified on the dull side. As others have observed as well,^[8] this side had been in contact with the rotating wheel. Optical microscopy inspections, X-ray diffraction (XRD), and electrical resistivity measurements, performed following a preliminary series of cathodic chargings, did not reveal any difference between the effects of hydrogen on the near-surface material from both sides. Nevertheless, all results presented herein refer to the bright side of the ribbon.

Electrochemical hydrogen charging of the amorphous ribbons was performed in a solution of 0.1 N H_2SO_4 with 5 mg/L NaAsO_2 as a surface poison. This solution is often used as a catholyte for ferrous samples in electrochemical permeation experiments, due to the ease of the cathodic reaction for hydrogen evolution.^[9] All chargings were carried out galvanostatically at room temperature, applying current densities of 2 to 150 A/m^2 for 0.25 to 121 hours. Hydrogen desorption was studied by thermal desorption spectroscopy (TDS); the principles of this technique and the experimental setup are described in detail elsewhere.^[7] Electrochemical charging for these experiments was done in a solution of 3 pct NaCl (in D_2O) with 5 mg/L NaAsO_2 . This deuterium-based electrolyte was chosen to reduce the background noise.

N. ELIAZ, formerly Ph.D. Student, Department of Materials Engineering, Ben-Gurion University of the Negev, is Postdoctoral Fellow, H.H. Uhlig Corrosion Laboratory, Massachusetts Institute of Technology, Cambridge, MA 02139. D. ELIEZER, Professor, is with the Department of Materials Engineering, Ben-Gurion University of the Negev, Beer-Sheva 84105, Israel.

Manuscript submitted February 2, 2000.

Thermal data such as crystallization temperature (T_c) and enthalpy (ΔH) were measured with a differential scanning calorimeter (PERKIN-ELMER* DSC7) at a heating rate of

*PERKIN-ELMER is a trademark of Perkin-Elmer Physical Electronics, Eden Prairie, MN.

20 °C/min. Calibration was done using standard samples of pure indium and pure zinc. Samples were tested in gold crucibles (an empty crucible serving as a reference) in the temperature range from 30 °C to 600 °C under a nitrogen atmosphere. Hydrogenated samples were run three times in order to isolate the effect of hydrogen on the metastable material. Hydrogen evolution and transformation of the metastable phase to the stable crystalline phases were evident from the first run. The second run would then show the baseline for the crystalline material. A third run was performed to ensure that all hydrogen was desorbed during the first run (*i.e.*, the baselines obtained in the second and third runs were similar). The third run was then subtracted from the first run. For transmission electron microscopy (TEM), using a JEOL** JEM-200B operating at 150 kV and a

**JEOL is a trademark of Japan Electron Optics Ltd., Tokyo.

PHILIPS† CM200 operating at 200 kV, thin samples were

†PHILIPS is a trademark of Philips Electronic Instruments Corp., Mahwah, NJ.

polished in a solution of 2:1 CH₃OH:HNO₃ or 1:15:3 HClO₄:C₂H₅OH:H₂O at -20 °C and 16 V. Some samples were thinned by ion milling at 5 kV and 0.9 mA for 2 hours. The XRD was carried out using a Rigaku D/Max-2100H diffractometer (Cu K α , $\lambda = 1.540562$ Å). Scanning electron microscopy (SEM) was used to determine the effect of hydrogen charging on the macrostructure and to characterize the fracture surfaces of brittle samples fractured during or immediately following hydrogen charging. Electrical resistivity measurements (using the four-point probe technique) were carried out at room temperature using a Keithley model 225 current supply (± 1 nA accuracy) and a Keithley model 195A digital multimeter (± 1 μ V). Microhardness testing was done with a Microduromat 4000E tester connected to a Reichert-Jung MeF-3 optical microscope. Measurements were performed at room temperature under a load of 35 gf, a loading rate of 10 gf/s, and a dwell time of 15 seconds.

III. RESULTS

A. Hydrogen Absorption

Visual inspections revealed that the ribbons gradually curled up in the solution during electrochemical charging. This curlup started after a certain initiation time and was especially significant under conditions of high current density or long charging time. If charging was stopped before the initiation of cracks and aging under room environment was performed, the original shape of the ribbon could be restored. However, with longer charging times, cracks initiated and propagated, ultimately leading to the disintegration of the sample in the solution—in the absence of external stresses. The kinetics of crack initiation and propagation became faster as the current density increased. These phenomena are similar to the ones reported for amorphous Fe₄₀Ni₃₈Mo₄B₁₈.^[10]

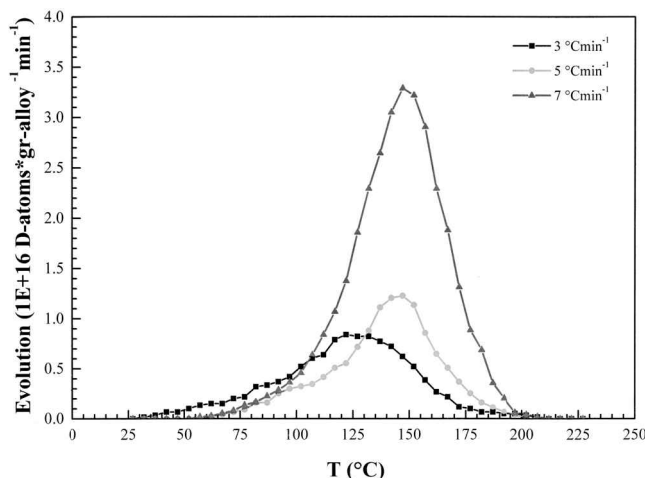


Fig. 1—Heating rate dependence of deuterium evolution from amorphous Fe₈₀B₁₁Si₉ charged at $i = 90$ A/m². Charging duration: 4 h.

An attempt was made to measure the amount of hydrogen absorbed in the material by weighing it before and immediately following charging, using a microbalance with an accuracy of ± 1 μ g. However, no weight increase was detected, probably due to the low solubility of hydrogen in this alloy. These findings are supported by TDS results, shown later in this article.

B. Hydrogen Desorption

Hydrogen desorption from the amorphous alloy was studied by means of TDS. Figure 1 shows the thermal desorption spectra at various heating rates. Table I summarizes some major parameters of hydrogen charging (current density and duration) and TDS (heating rate (φ)) from which the spectra presented in Figure 1 were obtained. This table also summarizes the values of several parameters characterizing the desorption of hydrogen from the amorphous alloy. The temperature at the desorption peak (T_c) and the maximal desorption rate were read directly from the spectra. The amount of hydrogen desorbed from the material within the investigated temperature range was obtained by integrating the plot of desorption rate *vs* time. The detailed procedure is described elsewhere.^[7] From Figure 1, it is evident that deuterium is desorbed from the material within the temperature range from 25 °C to 200 °C. A similar temperature range (73 °C to 217 °C) was reported^[11] for hydrogen desorption from amorphous Fe₇₉B₁₄Si₇, based on the appearance of an endothermic peak in the differential scanning calorimetry (DSC) plots of charged samples. Assuming that no deuterium remained inside the alloy at the end of the TDS experiments, the solubility of deuterium in amorphous Fe₈₀B₁₁Si₉ was measured to be $9.91 \cdot 10^{-6}$ to $1.84 \cdot 10^{-5}$ H/M. The effective activation energy for hydrogen release may be obtained by plotting the temperature of the desorption peak *vs* heating rate.^[7] Following this procedure, a value of $E_{aT} = 31.84 \pm 5.79$ kJ/mol (0.33 ± 0.06 eV/atom) was calculated.

C. Hydrogen Embrittlement

In this section, certain macroscopic and microscopic characteristics of the HE of amorphous Fe₈₀B₁₁Si₉ are presented.

Table I. Experimental Conditions of Hydrogen Charging and Thermal Desorption Experiments, as well as Values of Trapping Parameters Extracted from the TDS Spectra for an Amorphous Fe₈₀B₁₁Si₉ Alloy

Charging Conditions i (A/m ²), t (h)	Heating Rate φ (°C/min)	Temperature at Desorption Peak T_c (°C)	Maximum Desorption Rate (atoms/s)	Amount Desorbed (H/M)
$t = 4, i = 90$	3	122	$2.41 \cdot 10^{12}$	$1.52 \cdot 10^{-5}$
$t = 4, i = 90$	5	145	$3.47 \cdot 10^{12}$	$9.91 \cdot 10^{-6}$
$t = 4, i = 90$	7	149	$1.09 \cdot 10^{13}$	$1.84 \cdot 10^{-5}$

Since the embrittlement phenomenon has already been discussed in detail in a complementary article,^[5] this section mainly presents SEM observations that were not included in the previous article and explains in more detail the applicability of the high-pressure bubble-formation model to the amorphous material.

Figure 2(a) presents a SEM micrograph from the cross-section of an uncharged ribbon. Three voids, about 0.4 to 1.3 μm in diameter, which were formed during the preparation of the ribbon by rapid solidification, are evident. Such micron-sized voids were identified by Latanision *et al.*^[12] as typical in amorphous metals. No other defects (*e.g.*, cracks) were observed in the uncharged sample. Figure 2(b) shows a typical SEM micrograph from the surface of a sample charged at 20 A/m² for 30 minutes. A series of voids and interconnecting cracks are observed. Cracks interconnecting the voids were also observed by Latanision *et al.*^[12] in amorphous Fe₄₀Ni₄₀P₁₄B₆ following electrochemical permeation experiments. Figure 2(c) shows a typical micrograph from the surface of a sample charged at 100 A/m² for 30 minutes. More-severe damage is exhibited on the surface, as reflected by the higher density of voids and cracks, an increase in the mean diameter and opening of cracks, and by voids in the shape of blown bubbles. Figure 2(d) shows the fracture surface of a sample fractured during charging at 50 A/m². Shear bands, voids, and interconnecting cracks are observed, indicating that the defects observed in Figures 2(b) and (c) are not surface artifacts. Figure 2(e) presents a region from the fracture surface of a sample that was charged at 150 A/m² for 1 hour and intentionally fractured by applying an excessive bending force. Near the sample edge, a vein pattern is observed, typical of heterogeneous deformation of amorphous metals in the absence of hydrogen. Spaepen and Turnbull^[13] and Spaepen^[14] suggested that external shear stresses and internal stress concentrators might increase the free volume and the compositional disorder, thus causing a local softening of the material and forming a vein pattern. Near the center of the sample, however, a relatively small area of the fracture surface contains a cellular pattern. Similar cellular patterns were observed^[15-19] at the fracture surfaces of other amorphous alloys after hydrogen charging. The cellular pattern may be related to hydrogen embrittlement due to heterogeneous nucleation of local plastic deformation (*i.e.*, the fracture front propagates while coalescing small voids formed by hydrogen).

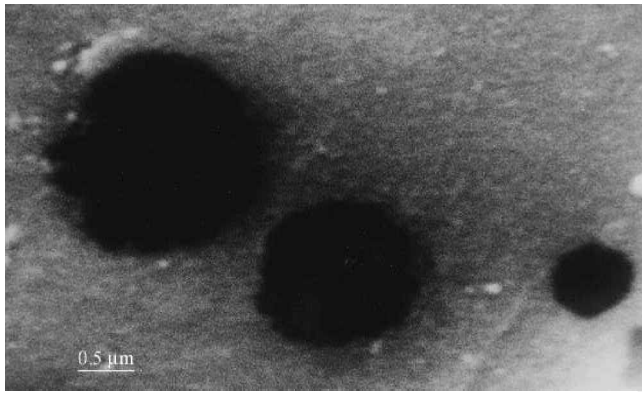
It should be noted that no change in microhardness was observed after hydrogenation. The distribution of hardness values for the uncharged ribbon (1024 to 1080 Vickers hardness number (VHN)) could not be distinguished from the distribution for the charged ribbons (969 to 1096 VHN). Nagumo and Takahashi^[15] were also not able to detect any

changes in microhardness following hydrogenation of amorphous Fe₇₀Cr₁₀P₁₃C₇ and Fe₈₀P₁₃C₇ alloys. The absence of any detectable changes in microhardness may result from the low content of hydrogen in these materials. The low hydrogen content leads to weak interactions between internal stress fields and to occupancy of relatively large interstitial sites, which is equivalent to the occupancy of interstitial sites in crystalline metals by smaller interstitials. Various mechanical properties of brittle materials may be estimated by insertion of microhardness indentations to the material and characterization of the Palmqvist, radial, or median cracks that are formed around them.^[20,21] Since this technique is appropriate for thin samples, an attempt was made to apply it for evaluating the effect of hydrogen on the fracture toughness (K_{IC}) of the alloy. Unfortunately, no cracks were observed around the indentations made in hydrogenated samples, although, macroscopically, it was clear that the material had become significantly brittle. This was probably due to the very low indenting loads applied on the thin ribbon in order to satisfy geometrical constraints. The ineffectiveness of the techniques based on insertion of microindentations led to the novel utilization of laser-induced shock-wave measurements of the dynamic spall strength, which ultimately supported the mechanism of high-pressure bubble formation.^[5]

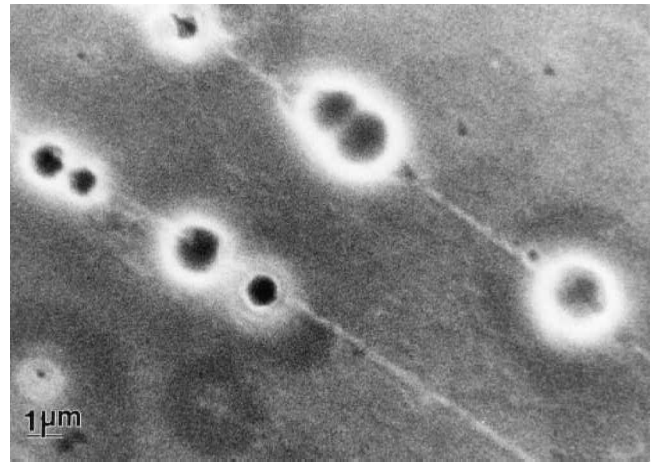
D. Hydrogen Effects on the Microstructure and Thermal Stability

Hydrogen effects on the microstructure and thermal stability of amorphous Fe₈₀B₁₁Si₉ were studied by XRD, DSC, TEM, and electrical resistivity measurements. Figure 3 shows the effect of hydrogenation ($i = 50$ A/m² and $t = 40$ min) on the XRD pattern. The existence of halos in the pattern of the uncharged sample is typical of amorphous materials and reflects the short-range order. A small broadening (in which the full width at half maximum increases from 4.53 to 4.94 deg) of the first halo is evident for the charged sample. On the basis of SEM observations, this broadening may be related to the stress fields or internal strains around defects (such as voids and cracks) that form in the material during hydrogenation. More interesting, however, is the observation of a shift of the first halo toward higher angles, reflecting a decrease in the mean distance between the nearest-neighbor atoms. These results could be reproduced a year later, supporting the authenticity of this uncommon phenomenon. Finally, no indications of hydrogen-induced phase separation are evident in Figure 3.

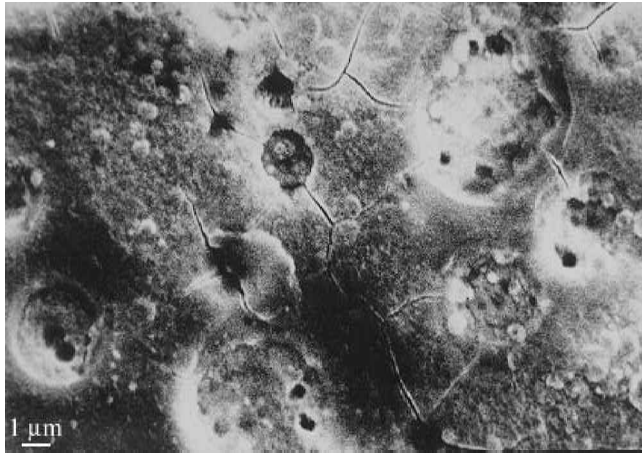
Figure 4(a) presents a typical TEM bright-field image and selected-area electron diffraction (SAED) pattern of the uncharged amorphous material. Amorphism was assured by



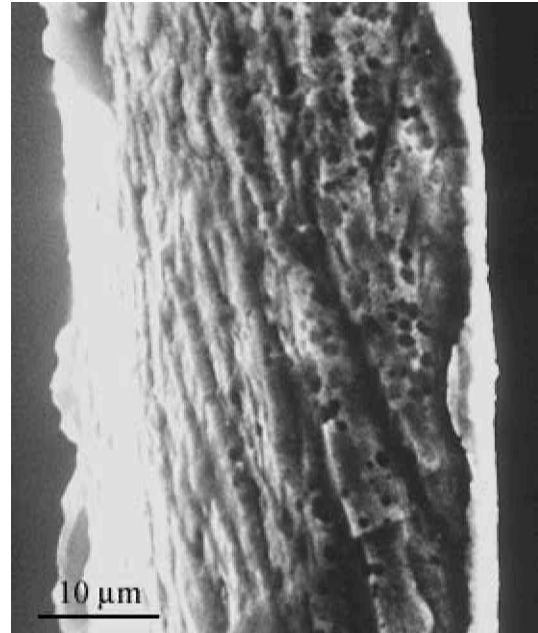
(a)



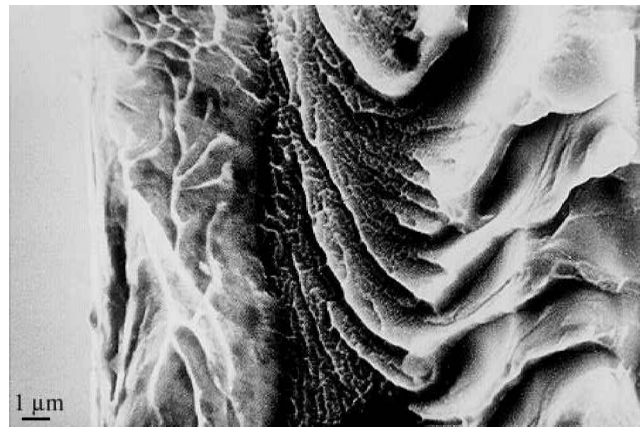
(b)



(c)



(d)



(e)

Fig. 2—SEM observations of hydrogen embrittlement of amorphous Fe₈₀B₁₁Si₉. (a) Internal voids at the cross-section of the as-received ribbon. (b) The surface of the ribbon after electrochemical charging at $i = 20 \text{ A/m}^2$ for 30 min. (c) The surface of the ribbon after charging at $i = 100 \text{ A/m}^2$ for 30 min. (d) The fracture surface of a sample, shattered during charging at $i = 50 \text{ A/m}^2$. (e) The fracture surface of a sample charged at $i = 150 \text{ A/m}^2$ for 1 h and fractured by hand bending.

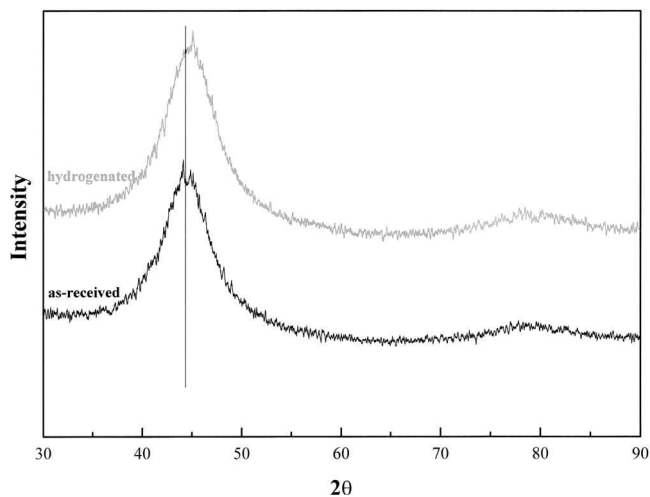
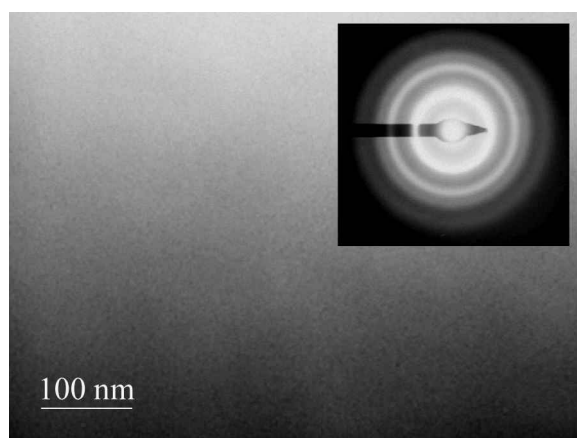
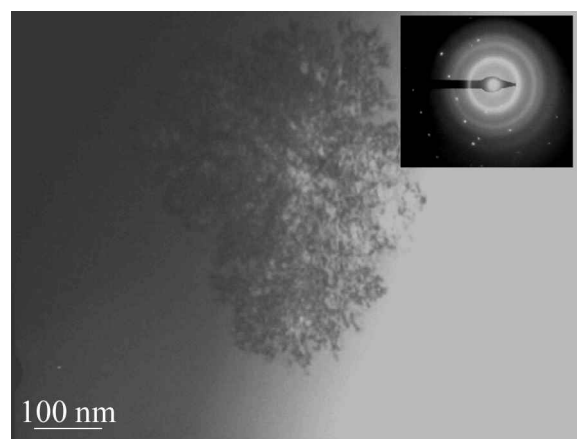


Fig. 3—X-ray diffraction patterns for as-received and hydrogenated ($i = 50 \text{ A/m}^2$, and $t = 40 \text{ min}$) glassy $\text{Fe}_{80}\text{B}_{11}\text{Si}_9$ ribbons.



(a)



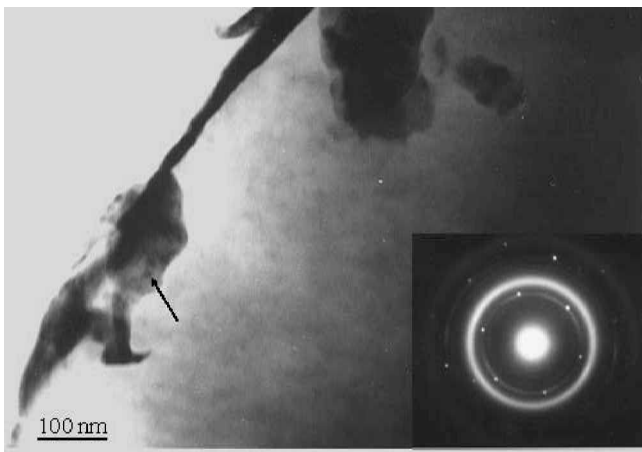
(b)

Fig. 4—TEM BF and SAED for the as-received ribbon: (a) amorphous matrix, and (b) nanocrystalline phase.

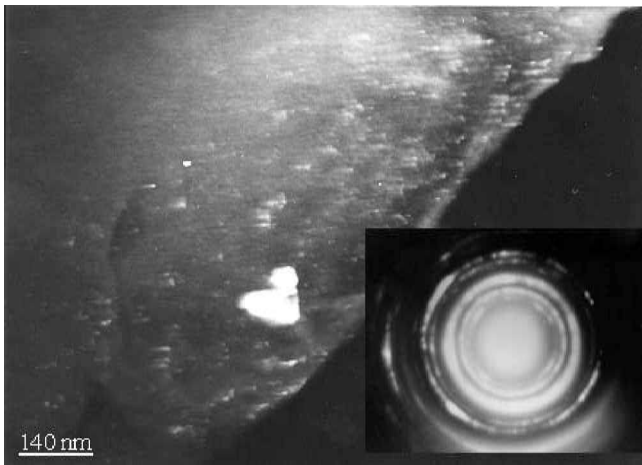
tilting the sample at high angles (up to 35 deg) and confirming the absence of change in the image contrast. The SAED pattern reveals a central bright area and several diffusive rings, typical of an amorphous phase. The central bright area contains the electrons that passed straight through the thin

sample. The origin of the diffusive rings is in electrons that were elastically scattered. The uniformity of the rings results from uniform radial scattering of electrons, as expected from a random structure. It should be noted that in some of the samples, evidence of chemical and/or structural inhomogeneity in the amorphous ribbon was observed. This evidence included areas of sharp black and white contrast, holes whose shape indicates a nonuniform response of the material to the thinning process, and either a nonuniform intensity of the diffusive ring or incomplete diffusive rings in the SAED patterns. On the basis of an absence of change in the image tone during tilting and SAED, the origin of the dark tone in different areas was determined to be the local thickness of the sample. A nonuniform intensity of the diffusive ring may result from either clusters of atoms with different atomic-scattering coefficients or local oxidation. It should be emphasized that before mounting the samples in the microscope, they were exposed to a short (30 minute) ion milling in order to remove oxides and impurities from the surface. An incomplete diffusive ring was proven to be an edge effect by comparing it with SAED patterns taken from the edge of the main hole. In one of the uncharged samples, even certain nanocrystallinity could be detected (Figure 4(b)). In order to identify the crystalline phase, JCPDS-ICDD cards were examined for different combinations of the elements Fe, B, Si, and O. A complete reflections list was obtained for known crystallographic structure and lattice parameters using CRYSTAL 3.0, a software package developed at Ben-Gurion University. A good fit of both the value of the spacing between the parallel planes and the angle between two Bragg's vectors was obtained when comparing this to the tetragonal phase $\text{Fe}_{\sim 3.5}\text{B}$, with lattice parameters of $a = b = 8.62 \text{ \AA}$ and $c = 4.28 \text{ \AA}$.^[22] However, the possibility of the formation of a crystalline phase that has not been reported cannot be excluded.

Figure 5 presents the microstructural characteristics at two different regions of a hydrogenated sample ($i = 50 \text{ A/m}^2$ and $t = 40 \text{ min}$). In one region (Figure 5(a)), distinct diffraction spots are evident in the SAED. The crystalline region from which the diffraction was taken (marked by an arrow) is surrounded by an amorphous region of dark tone (edge fold). In the second area (Figure 5(b)), new diffraction rings are evident. A careful examination reveals that in certain cases these rings are composed of discrete spots, while in other cases only segments of incomplete rings are evident. The identification of discrete diffraction spots indicates the existence of large-enough crystallites. Incomplete rings may result from a similar orientation of the crystallites as well as from an edge effect. The dark-field image (Figure 5(b)) also supports the existence of crystallites. One should note that the observed astigmatism results from the magnetic behavior of the material. By measuring the radii of the diffusive rings in Figures 5(a) and (b), an average distance of 2.032 to 2.043 Å between the first nearest-neighbor atoms in the amorphous structure was calculated. These values are in accordance with the values obtained from XRD measurements. Using the aforementioned procedure, the crystalline phase in the hydrogenated sample was found to be a cubic Fe_{23}B_6 phase with a lattice parameter of $a = 10.67 \text{ \AA}$.^[22] The values of the distances between the parallel planes, calculated on the basis of measuring the radii of the first five diffraction rings in Figure 5(a), were in accordance with



(a)



(b)

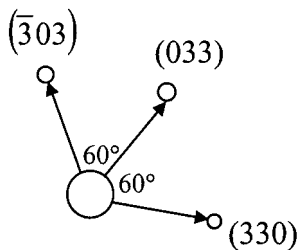


Fig. 5—TEM of hydrogenated ($i = 50 \text{ A/m}^2$, and $t = 40 \text{ min}$) amorphous $\text{Fe}_{80}\text{B}_{11}\text{Si}_9$ alloy. (a) BF image and SAED pattern from one region; and (b) DF and SAED pattern from a second region. Indexing of several reflections from the cubic Fe_{23}B_6 is also shown.

the reflections list for the Fe_{23}B_6 phase. Again, however, one cannot exclude the possibility of the formation of a new crystalline phase not yet reported. Figure 5 includes the indices of several reflections and the angles between Bragg's vectors for the possible Fe_{23}B_6 phase.

The electrical resistivity of a material is sensitive to changes in its electronic and/or microscopic structure. Figure 6 shows the effect of hydrogen charging on the electrical resistivity of amorphous $\text{Fe}_{80}\text{B}_{11}\text{Si}_9$, as measured by the four-point probe technique. The resistivity increased with charging current density. At high current densities (100 and 150 A/m^2), the resistivity increased with charging time; at

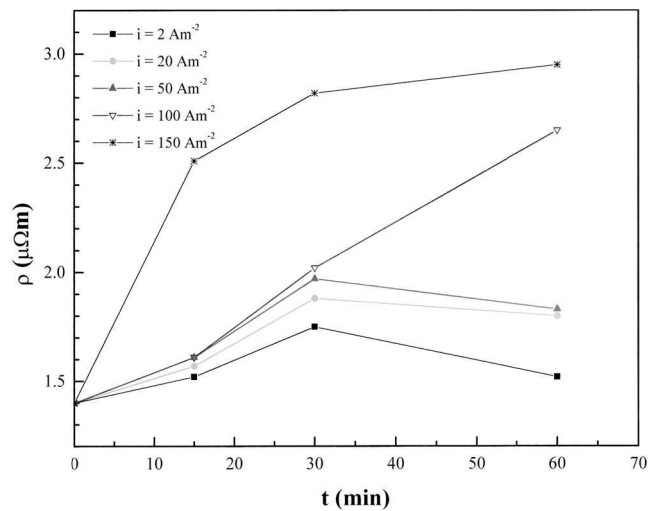


Fig. 6—The influence of current density and duration of hydrogen charging on the electrical resistivity of amorphous $\text{Fe}_{80}\text{B}_{11}\text{Si}_9$ ribbons.

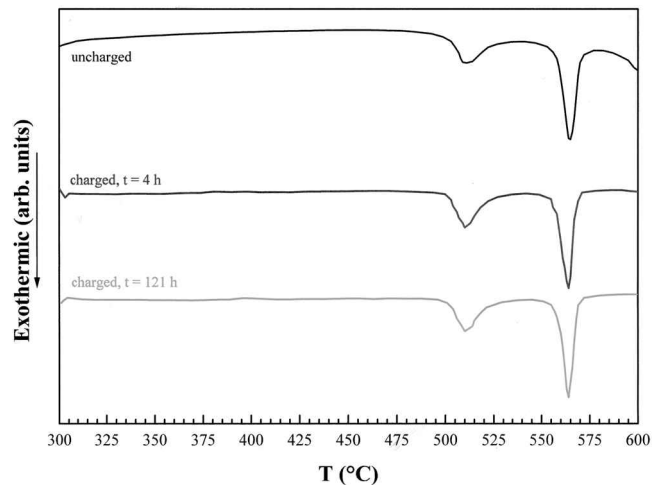
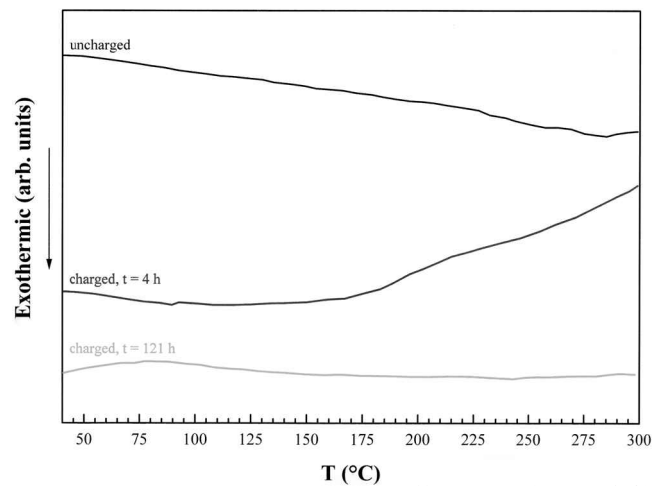


Fig. 7—DSC plots of uncharged and hydrogenated $\text{Fe}_{80}\text{B}_{11}\text{Si}_9$ glasses. Heating rate: $20 \text{ }^\circ\text{C/min}$; and charging current density: 10 A/m^2 .

lower current densities (2 to 50 A/m^2), a peak occurred after 30 minutes of charging.

Figure 7 shows the effect of hydrogenation on the DSC

plots. Since separate runs were carried out up to 300 °C and from 300 °C to 600 °C, the figure is divided into two (unmatched) parts. Two exothermic peaks were observed. By comparing these to the two-stage crystallization of metallic glasses of similar chemical composition, it is likely that the origin of the first peak was primary crystallization of α -Fe or α Fe(Si) having a bcc structure. The origin of the second peak was probably a secondary (eutectic) crystallization of Fe_2B .^[11,23,24] In the plots of some of the hydrogenated samples, an endothermic peak appeared at low temperatures (note, for example, the temperature range from 47 °C to 140 °C in the plot of a sample charged for 121 hours). Such an endothermic peak was not observed in the plots of uncharged samples. On the basis of TDS results, the endothermic peak may be related to hydrogen evolution from the sample. Similar endothermic transitions have been related to hydrogen desorption from other alloys.^[25] Only a slight decrease in the temperatures of the crystallization peaks, on the order of the calorimeter accuracy, was observed for the hydrogenated samples. Furthermore, no effect of hydrogen on the two-stage character of crystallization was evident.

IV. DISCUSSION

A. Hydrogen Absorption and Desorption

Electrochemical hydrogen charging of the amorphous ribbons was observed to be accompanied by a curling-up phenomenon. Surprisingly, although observed by other researchers as well, no explanation has been suggested for this phenomenon. One should note that, as a result of the disorder in the amorphous structure, atomic-scale stress fields exist in it, reflecting different local symmetries and topologies.^[26,27] The authors, thus, believe that the curling-up of amorphous ribbons during hydrogenation may result either from preferred penetration of hydrogen through one side of the ribbon (due to relatively high local tensile stresses on this side) or from the ribbon response to redistribution of the internal stress fields by hydrogen.

Weight measurements did not detect any weight increase following hydrogenation, probably due to the low solubility ($9.91 \cdot 10^{-6}$ to $1.84 \cdot 10^{-5}$ *H/M*) of hydrogen in an amorphous $\text{Fe}_{80}\text{B}_{11}\text{Si}_9$ alloy as measured by TDS. It has already been reported^[28] that hydrogen solubility in amorphous alloys that do not contain hydride-forming elements is relatively low and difficult to measure. On the other hand, hydrogen solubility in amorphous alloys that contain hydride-forming elements may be fairly high. For example, a hydrogen content as high as 1.0 *H/M* could be detected by weight measurements in amorphous $\text{Zr}_{69.5}\text{Cu}_{12}\text{Ni}_{11}\text{Al}_{7.5}$ following electrochemical charging at room temperature.^[29]

The effect of chemical composition on the characteristics of hydrogen absorption and desorption may be estimated by comparing the TDS results for the Fe-Si-B and Zr-Cu-Ni-Al systems (compare Figure 1 with Figure 8). Not only does the presence of hydride-forming elements lead to a much higher hydrogen solubility in the latter system, the temperatures at which desorption takes place are also significantly increased (350 °C to 700 °C for the latter).^[7] These two differences may be explained in terms of the heat of solution for hydrogen in these two systems. While zirconium is characterized by an exothermic enthalpy of solution for hydrogen

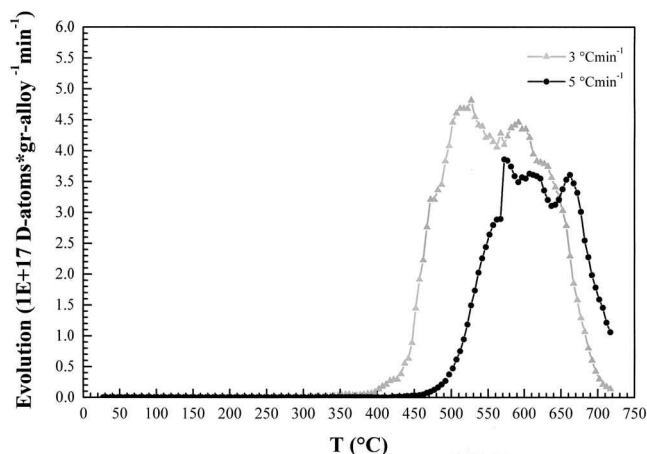


Fig. 8—Heating rate dependence of deuterium evolution from amorphous $\text{Zr}_{69.5}\text{Cu}_{12}\text{Ni}_{11}\text{Al}_{7.5}$ charged at $i = 100$ A/m². Charging duration: 4 h.^[7]

(−59.5 kJ/mol for α Zr), iron is characterized by endothermic enthalpy (+24.3 and +29.9 kJ/mol for α Fe and γ Fe, respectively).^[30]

Apparently, deuterium desorption from amorphous $\text{Fe}_{80}\text{B}_{11}\text{Si}_9$ is characterized by a single peak. Such behavior may result from the existence of sites of approximately the same energy for chemical interaction with hydrogen. Consequently, the energy levels of interstitial sites for hydrogen are determined mainly by the elastic strain energy, *i.e.*, by void size. A similar behavior was reported^[31] for hydrogen desorption from amorphous $\text{Fe}_{40}\text{Ni}_{38}\text{Mo}_4\text{B}_{18}$ and was attributed to the similar affinity to hydrogen of the elements surrounding the interstitial sites in this alloy. However, a careful examination of the change in the shape of the desorption profile for amorphous $\text{Fe}_{80}\text{B}_{11}\text{Si}_9$ at low heating rates reveals that different kinds of sites may eventually exist, the desorption from which may be distinguished only at very low heating rates. The appearance of secondary peaks may indicate that hydrogen diffusion and/or trapping is affected by local chemical heterogeneities in the amorphous material, as explained later.

The value of the effective activation energy for hydrogen release ($E_{aT} = 31.84 \pm 5.79$ kJ/mol) calculated in Section III is similar to the one reported for hydrogen trapping in microvoids in crystalline metals (37.63 kJ/mol).^[32] Therefore, it may be used to support the mechanism of high-pressure bubble formation for HE in amorphous $\text{Fe}_{80}\text{B}_{11}\text{Si}_9$, as suggested elsewhere.^[5] It should also be noted that the value of E_{aT} reported herein is higher than the value of activation energy for hydrogen desorption from amorphous $\text{Fe}_{79}\text{B}_{14}\text{Si}_7$ (21.23 ± 0.96 kJ/mol), as calculated elsewhere^[11] by applying Kissinger's equation to the endothermic peak in the DSC plots. On the other hand, the value reported herein is slightly lower than the value of the activation energy for hydrogen diffusion in amorphous $\text{Fe}_{78}\text{B}_{13}\text{Si}_9$ (37.63 ± 1.93 kJ/mol), as calculated^[33] on the basis of electrochemical permeation experiments. Any trial to explain these differences should be made with much caution. First, the values are not as different if one takes into account the different experimental techniques employed in the three cases. Second, for an amorphous structure, it may be more difficult to distinguish between the activation energy of diffusion and the activation energy of trapping/detrapping than

for a crystalline structure. Yet, one possible way to explain the different values is in terms of the slightly different chemical compositions. If similar diffusion processes in the amorphous structure are involved in all three studies, one can apply the model recently suggested by the authors to the diffusion of hydrogen in metallic glasses.^[4] This model describes the diffusion process of hydrogen in amorphous metals by means of an fcc-like quasi-lattice. Calculations of the interatomic interaction potential showed that alloying amorphous iron with either silicon or boron should result in an increase in the activation energy of hydrogen diffusion, the effect of silicon being more pronounced than the effect of boron at relatively high concentrations. Thus, changes in chemical composition are expected to lead to an increase in the activation energy of hydrogen diffusion when moving from Fe₇₉B₁₄Si₇ to Fe₈₀B₁₁Si₉ and, finally, to Fe₇₈B₁₃Si₉. This ranking is valid, however, only if two assumptions are fulfilled: first, similar hydrogen concentrations and temperatures should be common to all three studies, and, second, the effect of a 2 at. pct decrease in the silicon content should be more significant than an increase of 3 at. pct in the boron content at this concentration range.

B. Hydrogen Embrittlement

The SEM observations reported in Section III support the applicability of the high-pressure bubble-formation mechanism^[34] to explain the susceptibility of the amorphous Fe₈₀B₁₁Si₉ alloy to HE. Growth of internal traps, leading to HE of the amorphous Fe-Si-B alloy, is similar to the general description of Bockris and Reddy.^[35] Hydrogen absorbed in the material may reach internal surfaces, such as voids. Arriving at these regions, the hydrogen atoms adsorb on the surface and then form hydrogen molecules *via* chemical evolution. If the metal has an endothermic enthalpy for the hydrogen solution, the solubility of hydrogen in it will decrease as the temperature decreases. In addition, the metal will tend to allow precipitation of molecular hydrogen instead of maintaining electronic interaction with soluted hydrogen.^[36] Exposure of such a metal to high-fugacity hydrogen may lead to supersaturation and to the formation of bubbles, which serve as sinks for the excess hydrogen. Hydrogen diffusion toward the stress field around a bubble and precipitation of molecular hydrogen inside it lead to both bubble growth and pressure buildup inside it. When the pressure is high enough, the metal yields, and the bubble grows. If the bubble grows near the surface of the metal, a blister may form. Gas escape from the blister is eventually enabled by the collapse of its walls, a process accompanied by initiation of a crack at the surface. Crack initiation is catalyzed by the presence of an external stress. Therefore, there is a higher likelihood that cracks will initiate in regions of stress concentrations in the metal, since hydrogen moves preferably to them and penetrates into voids in their vicinity. If many voids exist in the material, hydrogen will be transported to them by diffusion, and cracks might propagate between them. The exposure of the material to stress will lead to brittle fracture along such cracks, instead of its yielding as a ductile material.

C. Hydrogen Effects on the Microstructure and Thermal Stability

In Section III, a shift of the first halo in the XRD pattern toward higher angles, as a result of hydrogen charging, was reported. To the best of the authors' knowledge, such a shift has not been reported before. Hydrogen charging usually causes a shift of the first halo to lower angles due to an increase in the distances between the first nearest-neighbor atoms and expansion of the material.^[1] This expansion may be explained in terms of occupation of interstitial sites in the amorphous metal by hydrogen atoms. In other cases, no shift of the first halo was observed after hydrogenation.^[11] The shift to higher angles may result from formation of atomic clusters of metal or metal-metalloid, up to nucleation of a crystalline phase, in the presence of hydrogen. Evidence supporting such a phenomenon was observed by TEM and electrical resistivity measurements. Alternatively, since the hydrogen concentration in this alloy is very low, the concept of Stolz *et al.*^[37] may be applied, according to which hydrogen can occupy only the relatively large interstitial sites. Since the Fe-Si-B system has very limited solubility and does not tend to form intermetallic phases, the interatomic interaction potential is expected to increase as the distances between atoms decrease.^[4] Therefore, when hydrogen occupies only the interstitial sites of large interatomic distances, it may attract the atoms surrounding it *via* electronic interactions.^[37] One should note that whatever the origin, the shift toward higher angles has to overcome competing influences, such as internal strains, which tend to shift the halo toward lower angles.

The results of electrical resistivity measurements may be explained in terms of defect formation and changes in the electron density during hydrogenation. As evident from the SEM micrographs, at high current densities macroscopic defects were formed, serving as scattering centers for conducting electrons; therefore, the resistivity increased gradually with charging time. At low current densities, on the other hand, changes in the electronic structure due to nanocrystallization and/or interaction between the hydrogen atoms probably led to a decrease in electrical resistivity after a certain time of charging.

The effect of hydrogenation on the electrical resistivity of amorphous alloys has been reported by others as well. Chelluri and Kirchheim^[38] investigated the effect of hydrogen on the electrical resistivity of amorphous Ni₆₄Zr₃₆, Pd_{77.5}Si_{16.5}Cu₆, and Pd₈₂Si₁₈ alloys. The increase in electrical resistivity per unit of hydrogen concentration was found to depend linearly on the logarithm of hydrogen concentration. Such behavior is different from that observed in crystalline materials, where the increase in electrical resistivity is not dependent on hydrogen concentration. Chelluri and Kirchheim related the behavior in the amorphous materials to the existence of energetically different sites for hydrogen accumulation as a function of hydrogen concentration in the alloy. Another conclusion was that the effect of hydrogen on the electrical resistivity is similar in amorphous alloys from the metal-metalloid and metal-metal groups. Fromageau *et al.*^[39] reported a similar effect of hydrogen on the electrical resistivity of an amorphous Pd₈₀Si₂₀ alloy. It should be noted that in both works, much smaller changes in electrical resistivity were measured following hydrogenation in comparison to those observed in the present work

(especially when the small concentrations of hydrogen in amorphous $\text{Fe}_{80}\text{B}_{11}\text{Si}_9$ are taken into account). Furthermore, a decrease in the electrical resistivity during hydrogenation was related in these works to hydride formation, which is irrelevant for the present study. Menzel *et al.*^[40] found hydrogen to significantly affect the electrical resistivity of amorphous binary Ni-Ti and Cu-Ti alloys. While in amorphous Cu-Ti alloys the resistivity approached a peak at a certain hydrogen concentration, in Ni-Ti alloys it gradually increased with hydrogen concentration until saturation. Finally, Lazarova *et al.*^[11] reported an increase in the electrical resistivity of amorphous $\text{Fe}_{79}\text{B}_{14}\text{Si}_7$ with charging time, according to a parabolic dependence.

Comparing the TEM results for the as-received and hydrogenated samples, the latter contained a crystalline phase that was not observed in the former. On the one hand, it cannot be excluded that either the same crystalline phase also exists in the uncharged ribbon or that it is a product of an interaction between hydrogen and another pre-existing crystalline phase such as $\text{Fe}_{\sim 3.5}\text{B}$. On the other hand, based on the results of XRD and electrical resistivity measurements, the crystalline Fe_{23}B_6 phase may be a product of hydrogen-induced crystallization of the amorphous matrix. Such nanocrystallization may explain the shift of the first halo in the XRD pattern toward higher angles. It may also explain the sudden decrease in electrical resistivity following hydrogenation under similar conditions. Even if such crystallization took place, the absence of any sharp peaks in the XRD pattern is still reasonable, as both the dimensions and the volume fraction of the new crystals are very small.

To the best of the authors' knowledge, crystallization of amorphous alloys as a result of electrochemical hydrogen charging at room temperature has not been previously reported. What has been reported, however, is a phase separation in the amorphous matrix, indicated in some cases by splitting of the original diffusive ring in the SAED pattern into two new diffusive rings (refer, for example, to Reference 41).

A new model is, thus, suggested herein to explain a possible hydrogen-induced crystallization in amorphous $\text{Fe}_{80}\text{B}_{11}\text{Si}_9$. As described before, some indications were observed by TEM of local chemical inhomogeneity in the uncharged amorphous alloy. Several researchers have reported chemical inhomogeneity in amorphous alloys. Piller and Haasen,^[42] for example, found a certain volume fraction of boron-rich clusters in amorphous $\text{Fe}_{40}\text{Ni}_{40}\text{B}_{20}$ by means of analytical field-ion microscopy. It has also been reported^[12] that regions of a local high concentration of metalloids (*e.g.*, boron) may serve as preferred sites for hydrogen diffusion. Hydrogen may reduce the stability of the amorphous phase by increasing the mobility of the alloy constituents.^[25] Hence, if the local concentration of hydrogen in boron-rich regions is high enough, a local crystallization of the amorphous phase to form a boron-rich crystalline phase may take place. The crystallization is driven by an increase in the free energy of the hydrogenated amorphous phase relative to the new crystalline phase. Indeed, the crystalline Fe_{23}B_6 phase is enriched in boron in comparison to the as-received alloy. Furthermore, as less amorphous phase is available for the regular crystallization reactions, they may release less heat (as was observed by DSC).

From TDS results, it is known that within the temperature

range from 500 °C to 570 °C, where this alloy crystallizes, no hydrogen is left in the material. This is apparently the reason for the absence of a hydrogen effect on the thermal stability, as evident from the DSC results. Similar behavior was reported for amorphous $\text{Fe}_{79}\text{B}_{14}\text{Si}_7$.^[11] It should be noted that, based on DSC results, the enthalpies of crystallization of amorphous $\text{Fe}_{80}\text{B}_{11}\text{Si}_9$ were found to be $\Delta H_{x1} = 41$ to 46 J/g, $\Delta H_{x2} = 74$ to 89 J/g, and $\Delta H_{\text{cryst}} = 5.7$ to 6.4 kJ/mol (the latter representing the sum of both stages). Surprisingly, the enthalpy of the second crystallization reaction was found to be less exothermic for the charged samples than for the as-received sample (74 to 76.5 and 89 J/g, respectively). This difference may result from the availability of less amorphous material to the crystallization reaction due to former nanocrystallization, as discussed previously. On the other hand, if more crystals exist in the hydrogenated samples, the absence of any other detectable effect of hydrogen on the DSC plots may result from the resolution limitation of the calorimeter or from the complexity of interfacial reactions involving nanocrystals.

V. CONCLUSIONS

Hydrogen effects on an amorphous $\text{Fe}_{80}\text{B}_{11}\text{Si}_9$ alloy were studied using a variety of advanced techniques. The following conclusions have been drawn.

1. Hydrogen-induced nanocrystallization in an amorphous alloy following electrochemical charging at room temperature has been possibly observed for the first time. This observation is supported by TEM, XRD, and electrical resistivity measurements. The driving force for such a crystallization may be the combination of local chemical inhomogeneity in the uncharged alloy and an increase in the free energy of the hydrogenated amorphous phase relative to the crystalline phase. However, one cannot exclude the possibility of a transformation of a pre-existing nanocrystalline phase.
2. The absence of hydride-forming elements in an amorphous $\text{Fe}_{80}\text{B}_{11}\text{Si}_9$ alloy results in low hydrogen solubility ($\sim 10^{-5}$ H/M) and low desorption temperatures (25 °C to 200 °C) in comparison to those of an amorphous $\text{Zr}_{69.5}\text{Cu}_{12}\text{Ni}_{11}\text{Al}_{7.5}$ alloy (up to 1.0 H/M and 350 °C to 700 °C, respectively).
3. The susceptibility of an amorphous $\text{Fe}_{80}\text{B}_{11}\text{Si}_9$ alloy to hydrogen embrittlement may be explained in terms of the high-pressure bubble-formation mechanism.

ACKNOWLEDGMENTS

The authors thank Dr. Arslan Kaya (Ben-Gurion University) and Mrs. Monika Meuris, Ms. Daniela Zander, and Professor Uwe Köster (Dortmund University) for their help in part of the TEM work. The professional assistance of Mrs. Zelda Bilbil in DSC experiments is greatly appreciated. Finally, the authors are grateful to Dr. Gary Leisk (MIT) for his constructive remarks.

REFERENCES

1. N. Eliaz and D. Eliezer: *Adv. Perf. Mater.*, 1999, vol. 6(1), pp. 5-31.
2. N. Eliaz: Ph.D. Thesis, Ben-Gurion University of the Negev, Beer-Sheva, Israel, 1999.

3. C.H. Bennett, D.E. Polk, and D. Turnbull: *Acta Metall.*, 1971, vol. 19, pp. 1295-98.
4. N. Eliaz, D. Fuks, and D. Eliezer: *Acta Mater.*, 1999, vol. 47(10), pp. 2981-89.
5. N. Eliaz, E. Moshe, S. Eliezer, and D. Eliezer: *Metall. Mater. Trans. A.*, 2000, vol. 31A, pp. 1085-93.
6. U. Köster and U. Schünemann: in *Rapidly Solidified Alloys*, H.H. Liebermann, ed., Marcel Dekker, New York, NY, 1993, pp. 303-37.
7. N. Eliaz, D. Eliezer, E. Abramov, D. Zander, and U. Köster: *J. Alloys Compounds*, 2000, vol. 305(1-2), pp. 272-81.
8. U. Köster, U. Herold, and H.-G. Hillenbrand: *Scripta Metall.*, 1983, vol. 17, pp. 867-72.
9. M.A.V. Devanathan, Z. Stachurski, and W. Beck: *J. Electrochem. Soc.*, 1963, vol. 110(8), pp. 886-90.
10. J.-J. Lin and T.-P. Perng: *Metall. Mater. Trans. A*, 1995, vol. A26, pp. 191-96.
11. M. Lazarova, T. Spassov, and S. Budurov: *Int. J. Rapid Solidification*, 1994, vol. 8(2), pp. 133-45.
12. R.M. Latanision, C.R. Compeau, and M. Kurkela: in *Hydrogen Embrittlement and Stress Corrosion Cracking*, R. Gibala and R.F. Hehemann, eds., ASM, Metals Park, OH, 1984, pp. 297-313.
13. F. Spaepen and D. Turnbull: *Scripta Metall.*, 1974, vol. 8(5), pp. 563-68.
14. F. Spaepen: *Acta Metall.*, 1977, vol. 25(4), pp. 407-15.
15. M. Nagumo and T. Takahashi: *Mater. Sci. Eng.*, 1976, vol. 23, pp. 257-59.
16. S. Ashok, N.S. Stoloff, M.E. Glicksman, and T. Slavin: *Scripta Metall.*, 1981, vol. 15, pp. 331-37.
17. T.K.G. Nambodhiri, T.A. Ramesh, G. Singh, and S. Sehgal: *Mater. Sci. Eng.*, 1983, vol. 61, pp. 23-29.
18. H.W. Schroeder and U. Köster: *J. Non-Cryst. Solids*, 1983, vol. 56, pp. 213-18.
19. J.-J. Lin and T.-P. Perng: *Metall. Mater. Trans. A*, 1995, vol. 26A, pp. 197-202.
20. K. Niihara, R. Morena, and D.P.H. Hasselman: *J. Mater. Sci. Lett.*, 1982, vol. 1 pp. 13-16.
21. K. Niihara: *J. Mater. Sci. Lett.*, 1983, vol 2, pp. 221-23.
22. U. Herold and U. Köster: *Z. Metallkd.*, 1978, vol 69, pp. 326-32.
23. R. Schulz, M.L. Trudeau, D. Dussault, A. Van Neste, and L. Dignard-Bailey: *Mater. Sci. Eng. A*, 1994, vols. A179-A180, pp. 516-20.
24. P.G. Caceres and K. Habib: *Z. Metallkd.*, 1996, vol. 87(4), pp. 300-04.
25. R.C. Bowman, Jr.: *Mater. Sci. Forum*, 1988, vol. 31, pp. 197-228.
26. V. Vitek and T. Egami: *Phys. Status Solidi B*, 1987, vol. 144, pp. 145-56.
27. T. Egami: *J. Non-Cryst. Solids*, 1988, vol. 106(1-3), pp. 207-10.
28. R.W. Lin and H.H. Johnson: *J. Non-Cryst. Solids*, 1982, vol. 51(1), pp. 45-56.
29. D. Zander, H. Leptien, U. Köster, N. Eliaz, and D. Eliezer: *J. Non-Cryst. Solids*, 1999, vols. 250-52, pp. 893-97.
30. E. Fromm and G. Hörz: *Int. Met. Rev.*, 1980, vols. 5-6, pp. 269-311.
31. J.B. Han, D.W. Kweon and J.-Y. Lee, *J. Non-Cryst. Solids*, 1989, vol. 108, pp. 216-20.
32. J.B. Condon and T. Schober: *J. Nucl. Mater.*, 1993, vol. 207, pp. 1-24.
33. Y. Sakamoto, K. Baba, W. Kubahashi, K. Takao, and S. Takayama: *J. Non-Cryst. Solids*, 1984, vols. 61-62, pp. 691-96.
34. A.S. Tetelman and W.D. Robertson: *Trans. TMS-AIME*, 1962, vol. 224, pp. 775-83.
35. J.O'M. Bockris and A.K.N. Reddy: *Modern Electrochemistry*, [vol. 2,] Plenum Press, New York, NY, 1970, pp. 1328-44.
36. R.A. Oriani: *Trans. Fusion Technol.*, 1994, vol. 26, pp. 235-66.
37. U. Stolz, U. Nagorny, and R. Kirchheim: *Scripta Metall.*, 1984, vol. 18(4), pp. 347-52.
38. B. Chelluri and R. Kirchheim: *J. Non-Cryst. Solids*, 1983, vol. 54(1-2), pp. 107-12.
39. R. Fromageau, A. Magnouche and N. Gerard: *Phys. Status Solidi A*, 1985, vol. a91(1), pp. K75-K80.
40. D. Menzel, A. Niklas, and U. Köster: *Mater. Sci. Eng. A*, 1991, vol. A133, pp. 312-15.
41. J. Garaguly, A. Lovas, Á. Cziráki, M. Reybold, J. Takács, and K. Wetzig: *Mater. Sci. Eng. A*, 1997, vols. A226-A28, pp. 938-42.
42. J. Piller and P. Haasen: *Acta Metall.*, 1982, vol. 30(1), pp. 1-8.